

# Model for continuously scanning ultrasound vibrometer sensing displacements of randomly rough vibrating surfaces

Purnima Ratilal,<sup>a)</sup> Mark Andrews, Ninos Donabed, Ameya Galinde, and Carey Rappaport  
Center for Subsurface Sensing and Imaging Systems, Northeastern University,  
Boston, Massachusetts 02115

Douglas Fenneman

U.S. Army RDECOM CERDEC Night Vision and Electronic Sensors Directorate,  
10221 Burbeck Road, Fort Belvoir, Virginia 22060

(Received 20 June 2006; revised 4 November 2006; accepted 6 November 2006)

An analytic model is developed for the time-dependent ultrasound field reflected off a randomly rough vibrating surface for a continuously scanning ultrasound vibrometer system in bistatic configuration. Kirchhoff's approximation to Green's theorem is applied to model the three-dimensional scattering interaction of the ultrasound wave field with the vibrating rough surface. The model incorporates the beam patterns of both the transmitting and receiving ultrasound transducers and the statistical properties of the rough surface. Two methods are applied to the ultrasound system for estimating displacement and velocity amplitudes of an oscillating surface: incoherent Doppler shift spectra and coherent interferometry. Motion of the vibrometer over the randomly rough surface leads to time-dependent scattering noise that causes a randomization of the received signal spectrum. Simulations with the model indicate that surface displacement and velocity estimation are highly dependent upon the scan velocity and projected wavelength of the ultrasound vibrometer relative to the roughness height standard deviation and correlation length scales of the rough surface. The model is applied to determine limiting scan speeds for ultrasound vibrometer measuring ground displacements arising from acoustic or seismic excitation to be used in acoustic landmine confirmation sensing. © 2007 Acoustical Society of America.

[DOI: 10.1121/1.2404623]

PACS number(s): 43.35.Yb, 43.20.Fn [TDM]

Pages: 863–878

## I. INTRODUCTION

Ultrasound based vibrometers are increasingly deployed to measure the displacement and velocity of vibrating surfaces, interfaces, or objects for a wide range of engineering applications.<sup>1</sup> For instance, in biomedical imaging, the ultrasound vibrometer is used to measure displacement of tissue stimulated to vibrate by various forms of mechanical or optical excitation.<sup>2</sup> The displacement measurement provides information regarding the elastic and other mechanical properties of the tissue from which its health can be inferred. In acoustic landmine detection,<sup>3–5</sup> ultrasound vibrometers are being investigated as an imaging sensor that measures displacement and velocity of ground excited to vibrate at low acoustic or seismic frequencies in order to confirm the presence or absence of mine-like targets.<sup>6–8</sup> In many applications, it is desirable for the vibrometer to be used in a *continuous* scan mode to rapidly comb through large areas of the surface or object under investigation. The presence of undulations or roughness on the surface often degrades the performance of the vibrometer for measuring surface displacements.

Here we develop analytic and numerical models to investigate the performance of an ultrasound vibrometer system to be used in *continuous* scan mode for measuring dis-

placements of a randomly rough vibrating surface. The motivation for this work is in acoustic land mine confirmation.<sup>3–5</sup> Both plastic and metallic mines are highly compliant with complex mechanical structure compared to naturally occurring sediment or objects on the ground.<sup>3–5</sup> When excited at low frequencies with acoustic or seismic waves, shallow buried mines vibrate with large amplitude oscillations and also exhibit resonance characteristics.<sup>5</sup> The contrasting displacement amplitude of buried mines relative to their natural surroundings indicates their presence or absence in a given area. Laser vibrometers have been deployed to comb through the ground surface under investigation to create a displacement or velocity image of the area that is used to infer the horizontally projected size and shape of a mine.<sup>5,9</sup> Laser-based vibrometers are susceptible to scattering by vegetation and ground roughness when used in continuous scan mode owing to the short wavelength of optical light. This degrades displacement estimation.<sup>7</sup> In acoustic landmine detection applications, confirmation of the presence of a buried mine has been achieved when the laser vibrometer scans at speeds of 5 cm/s.<sup>10</sup> Ultrasound vibrometers may provide advantages in situations where the scan speed is limited by speckle noise caused by the vibrometer scanning over the rough ground. This is because the ultrasound wavelength is roughly a thousand times larger than that of the laser and is therefore less susceptible to scattering from the rough ground. This has been verified experimen-

<sup>a)</sup>Electronic mail: purnima@ece.neu.edu

tally in Ref. 7. Ultrasound vibrometers can also provide penetration through grass<sup>7</sup> to directly image ground vibration without the need for these vibrations to be coupled to blades of grass as required<sup>10</sup> for a laser vibrometer. Laser vibrometers are also costly to deploy in an array configuration since a suite of seven to ten of these sensors would be needed on a vehicle to comb through a region at least 1 m wide. Ultrasound vibrometers, on the other hand, are much less expensive to deploy. The models developed here are used to determine sonar design parameters and measurement geometry that can be used to enhance measurement of ground displacement and velocity with a continuously scanning ultrasound vibrometer.

The basics of an ultrasound vibrometer are as follows. The ultrasound source transducer transmits a signal at the carrier frequency that is incident on a surface or object. The signal is then reflected or scattered off the surface to a receiving transducer. The measurement can be either monostatic or bistatic. The moving surface or object causes phase modulation of the received field upon reflection or scattering. Laser based approaches<sup>11</sup> for signal processing such as coherent interferometry are commonly applied to extract information regarding the displacement and velocity of the surface. Ultrasound vibrometers may also use an incoherent approach of directly measuring the Doppler shift spectra.<sup>12</sup> Lasers have a narrow collimated beam and the angle incident on and reflected from the surface is often approximated as each traveling in one planar direction.<sup>11</sup> The resulting phase shift of the reflected field is then assumed to be linearly related to ground motion. Ultrasound transducers typically illuminate larger regions of the surface with finite spot sizes determined by the beam pattern of the transducer. This leads to multiple angles incident and reflected from the surface causing the phase shift in the reflected field to become nonlinearly related to the surface motion. Additional complexities arise when the vibrometer is used in continuous scan mode over a rough surface. The motion of the vibrometer adds temporally varying noise arising from scattering over the rough surface that randomizes the amplitude and phase of the received ultrasound signal. This causes a degradation of the signal spectrum as we will illustrate, rendering both coherent and incoherent processing extremely challenging when the surface being scanned is extremely rough.

Here, we apply Green's theorem to develop a full-field model for the time-dependent ultrasound field reflected and scattered off a randomly rough vibrating surface for a scanning, bistatic, ultrasound vibrometer system. Kirchhoff's approximation is used to model the local reflection and scattering from the rough surface. The model incorporates the beam patterns of both the transmitting and receiving ultrasound transducers as well as the statistical properties of the rough surface. The roughness heights on the surface are assumed to follow a spatial random process. The rough surface is characterized by its reflection coefficient and a correlation function that depends on the standard deviation of the roughness heights and their correlation length scales. The reflection coefficient takes into account any absorption losses on the rough surface. The theory developed here is general and applicable for analyzing the performance of other types of

wave-based vibrometers for sensing velocities and displacements of rough surfaces, including laser-based and radar-based<sup>4,13</sup> systems.

The model is applied to determine the performance of a continuously scanning ultrasound vibrometer for measuring ground displacements under varying environmental conditions as a function of sonar design and measurement parameters. Simulations with the model indicate that scan speed and projected ultrasound wavelength are the two most sensitive parameters that determine the accuracy of the displacement measurement. When the ultrasound wavelength projected onto the surface is large in comparison to the surface roughness height standard deviation, the surface is considered to be smooth. Under such conditions, the ultrasound vibrometer can continuously scan the surface at relatively high speeds to yield accurate estimates of surface displacements using both coherent and incoherent data processing schemes. When the ultrasound wavelength projected onto the surface is small in comparison to the surface roughness height standard deviation, the surface is considered to be rough. Estimation of surface displacement can degrade significantly due to random scattering from the rough surface. The vibrometer system then has to be reconfigured to either transmit at lower frequencies so that the surface appears less rough or the scan speed has to be reduced. The model is applied to determine limiting scan speeds for an ultrasound vibrometer deployed as part of an acoustic landmine imaging sensor over naturally rough terrain consisting of either sand or gravel. Our analysis shows that for a 50 kHz ultrasound system, it is possible to attain scan speeds of 50 cm/s in coarse sand environments and 20 cm/s in gravel environments in order to detect ground displacements of at least 0.02  $\mu\text{m}$ . For medium and fine sands or silt environments, the scan speed can be larger than 50 cm/s.

The effects of rough surface scattering on the performance of laser and ultrasound vibrometers have been investigated experimentally by a number of researchers.<sup>7,10,14,15</sup> These investigations all report on the severe degradation that vibrometer motion over a rough surface causes to surface displacement and velocity estimation. In addition to translation, some of these experimental investigations also study the effect of yaw, pitch, and roll on vibrometer performance. The previous *theoretical* studies of vibrometer performance conducted by Rothberg<sup>14</sup> are based on using random number generators to simulate the time-dependent noise field received by a vibrometer from a rough surface. Their model is not based on scattering theory. They do not account for the full three-dimensional (3D) scattering interaction of the ultrasound wave field with the rough surface as we do here. As a consequence, these previous theories<sup>14</sup> cannot provide a fundamental approach for analyzing speckle properties measured by a vibrometer as a function of the measurable statistical characteristic of a rough surface such as its roughness height standard deviation and correlation length scale.

In Sec. II, we develop the time-dependent full-field model for the ultrasound field reflected off a randomly rough vibrating surface. The coherent and incoherent signal processing schemes for estimating displacement and velocities from the received field are summarized in Sec. III. A statis-

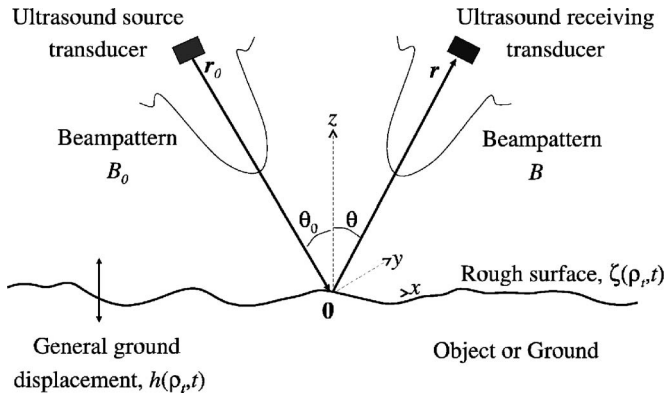


FIG. 1. Setup of a bistatic ultrasound vibrometer system. The origin of the coordinate system is located at the mean surface, at the intersection of the source and receiver beam-pattern axes.

tical description for the rough surface is provided in the Appendix and our approach for generating random realizations of the rough surface from its wave number spectrum is discussed in Sec. IV. Numerical simulations investigating the performance of the ultrasound vibrometer for application in landmine detection are provided in Sec. V.

## II. FULL-FIELD MODEL FOR ULTRASOUND SIGNAL REFLECTED OFF MOVING SURFACE WITH RANDOM ROUGHNESS

In this section, we develop an analytic model for the time-dependent ultrasound field reflected off a randomly rough vibrating surface for a scanning ultrasound vibrometer in bistatic configuration. The origin of the coordinate system is located at the mean surface. The  $z$  axis is normal to the mean surface, while the  $x$  and  $y$  axes are on the mean surface as illustrated in Fig. 1. The source transducer is located at  $\mathbf{r}_0 = (x_0, 0, z_0)$  and the axis of its main beam-pattern lobe makes an angle  $\theta_0 = \tan^{-1}(x_0/z_0)$  with the surface normal. The receiving transducer is located at  $\mathbf{r} = (x, 0, z)$  and its beam-pattern main lobe axis makes an angle  $\theta = \tan^{-1}(x/z)$  with the surface normal. We will assume throughout the paper that the peak amplitudes of the source and receiver beam patterns intercept the surface at the origin of the coordinate system. For an ultrasound vibrometer in scan mode, the origin of the coordinate system moves with the vibrometer. Coordinates of points on the rough surface are denoted by  $\mathbf{r}_t = (x_t, y_t, z_t)$ . Spatial cylindrical  $(\rho, \phi, z)$  and spherical  $(r, \theta, \phi)$  systems are defined by  $x = r \sin \theta \cos \phi$ ,  $y = r \sin \theta \sin \phi$ ,  $z = r \cos \theta$ , and  $\rho^2 = x^2 + y^2$ . The ultrasound frequency is denoted by  $f$ , with corresponding angular frequency  $\omega = 2\pi f$  and wave number  $k = \omega/c$  where  $c$  is the speed of sound in air.

For a continuously scanning ultrasound vibrometer, the surface imaged by the system within its resolution footprint can vary as a function of time as the vibrometer moves over the surface. Let the rough surface height at horizontal location  $\boldsymbol{\rho}_t = (x_t, y_t)$  on the surface imaged by the system at time instance  $t$  be given by  $\zeta(\boldsymbol{\rho}_t, t)$ . The  $x$  and  $y$  components of the gradient of the surface are, respectively,

$$p(\boldsymbol{\rho}_t, t) = \frac{\partial \zeta(\boldsymbol{\rho}_t, t)}{\partial x_t} \quad (1)$$

and

$$q(\boldsymbol{\rho}_t, t) = \frac{\partial \zeta(\boldsymbol{\rho}_t, t)}{\partial y_t}. \quad (2)$$

The surface normal can then be expressed as

$$\mathbf{n}(\boldsymbol{\rho}_t, t) = \frac{(p, q, 1)}{\sqrt{p^2 + q^2 + 1}}. \quad (3)$$

A statistical description of the surface roughness height  $\zeta$  is provided in the Appendix, along with its characterization in terms of a spatial correlation function and wave number spectrum.

For a vibrating rough surface, let  $h(\boldsymbol{\rho}_t, t)$  be the vertical displacement of the surface at location  $\boldsymbol{\rho}_t$  and at time  $t$ . Then the vertical position of the surface at  $\boldsymbol{\rho}_t$  at any time instance  $t$  is  $z_t = h(\boldsymbol{\rho}_t, t) + \zeta(\boldsymbol{\rho}_t, t)$ . The surface displacement  $h$  is a function of both space and time to account for local variations in the displacement of the surface within the ultrasound resolution footprint. This occurs in acoustic landmine detection when the ground is excited by short wavelength acoustic signals.

The incident and reflected ultrasound wave vectors are denoted by  $\mathbf{k}_i = k(\mathbf{r}_t - \mathbf{r}_0)/|\mathbf{r}_t - \mathbf{r}_0|$  and  $\mathbf{k} = k(\mathbf{r} - \mathbf{r}_t)/|\mathbf{r} - \mathbf{r}_t|$ , respectively. In general, these are functions of the source and receiver coordinates, respectively, as well as the coordinates of the surface since they determine the incident and reflected or scattered wave directions.

By application of Green's theorem, the time-dependent ultrasound field transmitted from a time harmonic source at  $\mathbf{r}_0$ , reflected off the surface and received at  $\mathbf{r}$  is<sup>16</sup>

$$P(\mathbf{r}, t) = \Re \left\{ e^{-i\omega t} \int \int_S w(\boldsymbol{\rho}_t) [\Phi(\mathbf{r}_t | \mathbf{r}_0) \nabla_t G(\mathbf{r} | \mathbf{r}_t) - G(\mathbf{r} | \mathbf{r}_t) \nabla_t \Phi(\mathbf{r}_t | \mathbf{r}_0)] \cdot \mathbf{n}(\boldsymbol{\rho}_t, t) dS_t \right\}, \quad (4)$$

where  $\Phi(\mathbf{r}_t | \mathbf{r}_0)$  is the total field on the surface,  $G(\mathbf{r} | \mathbf{r}_t)$  is the free space Green function given by

$$G(\mathbf{r} | \mathbf{r}_t) = \frac{1}{4\pi} \frac{1}{|\mathbf{r} - \mathbf{r}_t|} e^{ik \cdot (\mathbf{r} - \mathbf{r}_t)}, \quad (5)$$

$w(\boldsymbol{\rho}_t)$  is a window function that depends on the beam pattern  $B$  of the receiver projected onto the surface,

$$w(\boldsymbol{\rho}_t) = B \left( \sin^{-1} \frac{\rho_t \cos \theta}{\sqrt{(x - x_t)^2 + y_t^2 + z^2}} \right), \quad (6)$$

and  $S$  is the region of the surface that contributes to the integrand in Eq. (4). The beam patterns of the source and receiving transducers provide natural window functions to limit the dominant region of the surface, that contributes to the received field, to be located where the two main lobes of the transducers intersect the surface. This approach avoids the need to worry about problems arising from edge effects

when considering plane wave scattering from infinite surfaces as discussed in Ref. 17.

We apply Kirchhoff's approximation to estimate the total field on the surface as the sum of the incident and locally reflected fields,

$$\Phi(\mathbf{r}_t|\mathbf{r}_0) = Q(4\pi)^2 w_0(\boldsymbol{\rho}_t)(1 + R(\mathbf{k}_i, \boldsymbol{\rho}_t))G(\mathbf{r}_t|\mathbf{r}_0), \quad (7)$$

where  $Q$  is the source amplitude,  $w_0(\boldsymbol{\rho}_t)$  is the window function that determines the amplitude of the incident field at each point on the surface through the source beam pattern  $B_0$ ,

$$w_0(\boldsymbol{\rho}_t) = B_0 \left( \sin^{-1} \frac{\rho_t \cos \theta_0}{\sqrt{(x_0 - x_t)^2 + y_t^2 + z_0^2}} \right), \quad (8)$$

and  $R(\mathbf{k}_i, \boldsymbol{\rho}_t)$  is the local reflection coefficient on the surface. It depends on the intrinsic properties of the medium above and below the interface and the local curvature of the surface relative to the incident wave. For instance, in landmine detection applications, if the ground can be approximated as a homogeneous sediment, the reflection coefficient is

$$R(\mathbf{k}_i, \boldsymbol{\rho}_t) = \frac{\rho_2 \eta - \rho \sqrt{(k_2/k)^2 - (1 - \eta^2)}}{\rho_2 \eta + \rho \sqrt{(k_2/k)^2 - (1 - \eta^2)}}, \quad (9)$$

where  $\rho$  and  $\rho_2$  are the densities of air and ground, respectively,  $k_2 = 2\pi f/c_2$  is the ultrasound wave number on the ground,  $c_2$  is the compressional wave speed of the ground, and

$$\eta(\boldsymbol{\rho}_t, t) = \frac{\mathbf{k}_i \cdot \mathbf{n}(\boldsymbol{\rho}_t, t)}{k_i} \quad (10)$$

is the cosine of the angle between the incident field and the surface normal. The reflection coefficient is complex in general. It accounts for an absorptive surface or a lossy layer such as a layer of dense vegetation when  $|R| < 1$ .

The derivative of the Green function and that of the total field on the surface are, respectively,

$$\nabla_t G(\mathbf{r}|\mathbf{r}_t) = -ikG(\mathbf{r}|\mathbf{r}_t), \quad (11)$$

and

$$\nabla_t \Phi(\mathbf{r}_t|\mathbf{r}_0) = Q(4\pi)^2 w_0(\boldsymbol{\rho}_t) G(\mathbf{r}_t|\mathbf{r}_0) i(\mathbf{k}_i + \mathbf{k}' R(\mathbf{k}_i, \boldsymbol{\rho}_t)), \quad (12)$$

where  $\mathbf{k}'$  is the wave vector in the local reflection direction determined solely by the local incident wave vector and the surface normal. The dot product of the local incident and reflected wave vectors with the surface normal satisfy

$$\mathbf{k}_i \cdot \mathbf{n}(\boldsymbol{\rho}_t) = -\mathbf{k}' \cdot \mathbf{n}(\boldsymbol{\rho}_t). \quad (13)$$

Substituting Eqs. (5), (7), (11), and (12) into Eq. (4), and applying Eq. (13), we find

$$P(\mathbf{r}, t) = \Re \left\{ e^{-i\omega t} Q \int \int_S i [R(\mathbf{k}_i, \boldsymbol{\rho}_t)(\mathbf{k}_i - \mathbf{k}) - (\mathbf{k}_i + \mathbf{k})] \cdot \mathbf{n}(\boldsymbol{\rho}_t, t) w_0(\boldsymbol{\rho}_t) w(\boldsymbol{\rho}_t) \times G(\mathbf{r}_t|\mathbf{r}_0) G(\mathbf{r}|\mathbf{r}_t) dS_t \right\}. \quad (14)$$

Expressing the Green's function in Eq. (14) in terms of the surface coordinates, the ultrasound field reflected off the vibrating surface becomes

$$P(\mathbf{r}, t) = \Re \left\{ e^{-i\omega t} Q \int \int_{S_0} i [R(\mathbf{k}_i, \boldsymbol{\rho}_t)(\mathbf{k}_i - \mathbf{k}) - (\mathbf{k}_i + \mathbf{k})] \cdot \mathbf{n}(\boldsymbol{\rho}_t, t) w_0(\boldsymbol{\rho}_t) w(\boldsymbol{\rho}_t) \times \frac{\exp(ik\sqrt{(x_t - x_0)^2 + y_t^2 + (h(\boldsymbol{\rho}_t, t) + \zeta(\boldsymbol{\rho}_t, t) - z_0)^2})}{\sqrt{(x_t - x_0)^2 + y_t^2 + (h(\boldsymbol{\rho}_t, t) + \zeta(\boldsymbol{\rho}_t, t) - z_0)^2}} \times \frac{\exp(ik\sqrt{(x - x_t)^2 + y_t^2 + (z - h(\boldsymbol{\rho}_t, t) - \zeta(\boldsymbol{\rho}_t, t))^2})}{\sqrt{(x - x_t)^2 + y_t^2 + (z - h(\boldsymbol{\rho}_t, t) - \zeta(\boldsymbol{\rho}_t, t))^2}} dS_t \right\}. \quad (15)$$

Note that in Eq. (15), the phase of the received signal is a nonlinear function of the surface displacement  $h(\boldsymbol{\rho}_t, t)$ . This is in contrast to the field measured using a narrow collimated laser beam where the received signal phase is often approximated to be a linear function of the surface displacement.<sup>11</sup> The wave numbers  $k$  in the argument of the exponential terms in Eq. (15) are complex to account for attenuation due to absorption in air. The surface displacement is an arbitrary function of time and can be used to describe surface motion arising from both sinusoidal and broadband excitation. Besides the ultrasound vibrometer, the theory developed here is also applicable to other wave-based displacement sensors, including both laser and radar<sup>4,13</sup> vibrometers.

In order to illustrate the approaches for processing the received signal, we simplify Eq. (15) in the next section so that the received signal phase becomes a linear function of surface displacement. The conditions under which this simplification is valid for the ultrasound vibrometer is also discussed there. In Sec. V, we implement the full-field model in Eq. (15) for the general ultrasound vibrometer and numerically evaluate its performance for estimating surface displacement amplitudes and velocities under different environmental conditions and measurement scenarios.

*Narrow beamwidth approximation.* For an ultrasound vibrometer with a sufficiently narrow beamwidth such that the dominant ultrasound field incident on and reflected from the surface can each be approximated as traveling in one planar direction, much simplification can be obtained for the ultrasound field measured at the receiver. Let  $\rho_e$  be the radius of the patch of surface insonified by the transducer within its equivalent beamwidth,  $\theta_e$ . The ultrasound fields incident upon and reflected from the surface are approximately planar if the phase variation within the insonified region is less than  $\pi/4$ . This occurs for vibrometer systems that satisfy  $\theta_e < \sqrt{\lambda}/r$ . This is the required condition for the vibrometer in order for the analysis in this section to be applicable. We also assume that the beam-pattern main lobe axis of the source and receiving transducers are symmetric about the  $z$  axis so that  $\theta = \theta_0$ , and the wave vectors are each planar,  $\mathbf{k}_i \approx (k_x, 0, -k_z)$  and  $\mathbf{k} \approx (k_x, 0, k_z)$ , where  $k_x = k \sin \theta$  and  $k_z = k \cos \theta$ .

The argument within the exponential phase terms in Eq. (15) can be simplified following  $\mathbf{k}_i \cdot (\mathbf{r}_t - \mathbf{r}_0) = k\sqrt{(x_t - x_0)^2 + y_t^2 + (h(\boldsymbol{\rho}_t, t) + \zeta(\boldsymbol{\rho}_t, t) - z_0)^2} \approx -k_x x_0 - k_z(\zeta(\boldsymbol{\rho}_t) + h(t) - z_0)$ , while the spherical spreading terms approximated following  $|\mathbf{r}_t - \mathbf{r}_0| \approx r_0$ . The weighting functions on the surface can be approximated as step functions over an area delimited by the equivalent beamwidth of the source and receiver, for instance,

$$w(\boldsymbol{\rho}_t) = \begin{cases} 1 & \text{for } \rho_t < \rho_e \\ 0 & \text{elsewhere.} \end{cases} \quad (16)$$

We assume the local slopes on the surface are sufficiently small so that we can approximate the reflection coefficient over the insonified area as a constant,  $R(\mathbf{k}_i, \boldsymbol{\rho}_t) = R_0$ . Furthermore, we approximate  $(\mathbf{k}_i - \mathbf{k}) \cdot \mathbf{n}_t \approx -2k_z$  and  $(\mathbf{k}_i + \mathbf{k}) \cdot \mathbf{n}_t \approx 0$ . Equation (15) for the field measured by the receiving transducer then becomes

$$\begin{aligned} P(\mathbf{r}, t) &= -\Re \left\{ e^{-i\omega t} i Q 2k_z R_0 \int_0^{\rho_e} \int_0^{2\pi} \frac{1}{r_0} e^{-i[k_x x_0 + k_z(\zeta(\boldsymbol{\rho}_t, t) + h(t) - z_0)]} \frac{1}{r} e^{i[k_x x + k_z(z - \zeta(\boldsymbol{\rho}_t, t) - h(t))]} \rho_t d\phi_t d\rho_t \right\} \\ &= -\Re \left\{ e^{-i\omega t} i (4\pi)^2 Q 2k_z R_0 G(\mathbf{0}|\mathbf{r}_0) G(\mathbf{r}|\mathbf{0}) e^{-i2k_z h(t)} \int_0^{\rho_e} \int_0^{2\pi} e^{-i2k_z \zeta(\boldsymbol{\rho}_t, t)} \rho_t d\phi_t d\rho_t \right\}, \end{aligned} \quad (17)$$

where the last equality was obtained by applying Eq. (5).

We next denote the last factor in Eq. (17) which is the integrated random phase contribution to the reflected field due to scattering from roughness elements on the surface as

$$\mathcal{Z}_N(t) = A_N(t) e^{i\phi_N(t)} = \int_0^{\rho_e} \int_0^{2\pi} e^{-i2k_z \zeta(\boldsymbol{\rho}_t, t)} \rho_t d\phi_t d\rho_t. \quad (18)$$

Note that random scattering from surficial roughness affects both the amplitude and phase of the reflected signal so that both  $A_N$  and  $\phi_N$  are random variables, or equivalently,  $\mathcal{Z}_N$  is a complex random variable. They may also be functions of time depending on whether the vibrometer is stationary in space or moving across the surface. Substituting Eq. (18) into Eq. (17), we obtain

$$\begin{aligned} P(\mathbf{r}, t) &= \Re \{ B \mathcal{Z}_N(t) e^{-i(\omega t + 2k_z h(t))} \} \\ &= \Re \{ B A_N(t) e^{-i[\omega t + 2k_z h(t) - \phi_N(t)]} \}, \end{aligned} \quad (19)$$

where  $B = -i(4\pi)^2 Q 2k_z R_0 G(\mathbf{0}|\mathbf{r}_0) G(\mathbf{r}|\mathbf{0})$ .

Under the narrow beamwidth approximation, the phase of the received signal becomes a linear function of the surface displacement  $h(t)$ . This linear dependence is also obtained when one makes the far-field approximation.<sup>25</sup> Equation (19) is now directly amenable to both coherent and incoherent signal processing approaches for estimating surface displacement and velocity amplitudes as discussed next.

### III. ULTRASOUND SIGNAL ANALYSIS FOR SURFACE DISPLACEMENT AND VELOCITY ESTIMATION

A review of approaches used to analyze ultrasound sensor data to estimate surface displacement and velocity for a wide range of applications is provided in the introduction of Ref. 12. They can be grouped into two main categories—either incoherent Doppler shift spectra or coherent interferometry. In the following, we discuss a version of each of these two main approaches for analyzing ultrasound sensor data by applying them analytically to the narrow beamwidth ultrasound system to estimate surface displacement. These

approaches are also applied to analyze full-field data from the general larger beamwidth ultrasound system in the numerical simulation examples of Sec. V.

#### A. Incoherent Doppler shift spectra

This approach analyzes the signal received at the ultrasound transducer incoherently. For time-harmonic sinusoidal oscillations of the surface, it provides an estimate of the amplitude of the surface displacement from the spectrum of the received ultrasound field. We consider two specific motions of the surface—uniform translation and sinusoidal oscillation about a mean position.

For uniform translation of the surface, the speed  $v_g$  of the surface is a constant and the displacement can be expressed as

$$h(t) = v_g t. \quad (20)$$

Substituting Eq. (20) into Eq. (19), the field measured by the transducer becomes

$$P(\mathbf{r}, t) = \Re \{ B \mathcal{Z}_N(t) e^{-i(\omega + 2k_z v_g) t} \}. \quad (21)$$

In the absence of time-dependent scattering from the rough surface, the Fourier transform  $P(\omega')$  of the received ultrasound signal defined as

$$P(\omega') = \int_0^T P(\mathbf{r}, t) e^{i\omega' t} dt \quad (22)$$

has a shift in the peak frequency from  $\omega' = \omega$  to  $\omega' = \omega + 2k_z v_g$ . This Doppler shift in peak frequency  $2k_z v_g = 2k v_g \cos \theta$  is directly proportional to the projected velocity  $v_g \cos \theta$  of the surface in the direction of the transducer beam. For this approach to work, the projected surface velocity must be large enough to resolve the shift in peak frequency. In Eq. (22),  $T$  is the time duration of the signal used for computing its Fourier transform.

We next consider sinusoidal oscillations of the surface at angular frequency  $\omega_g$  where the displacement can be expressed as

$$h(t) = h_0 \cos(\omega_g t + \phi_g). \quad (23)$$

Substituting Eq. (23) into Eq. (19), the field measured by the receiving transducer becomes

$$P(\mathbf{r}, t) = \Re\{B\mathcal{Z}_N(t)e^{-i[\omega t + 2k_z h_0 \cos(\omega_g t + \phi_g)]}\}. \quad (24)$$

Following the approach of Refs. 2, 11, and 7, we expand the sinusoidal phase term in Eq. (24) as a Bessel series of the form,  $e^{ia \cos b} = \sum_{n=-\infty}^{\infty} i^n J_n(a) e^{inb}$ , to obtain

$$P(\mathbf{r}, t) = \Re\left\{B\mathcal{Z}_N(t) \sum_{n=-\infty}^{\infty} i^n J_n(2k_z h_0) e^{i[(n\omega_g - \omega)t + n(\phi_g + \pi)]}\right\}. \quad (25)$$

We next take the Fourier transform of Eq. (25) following Eq. (22). Note that if the time-dependent variation in the scattering from the rough surface is negligible, the ratio of the Fourier transform peak magnitude at  $\omega' = \omega$  to the  $n$ th order sideband at  $\omega' = \omega \pm n\omega_g$  can be approximated as

$$\frac{|P(\omega' = \omega)|}{|P(\omega' = \omega \pm n\omega_g)|} = \frac{|J_0(2k_z h_0)|}{|J_n(2k_z h_0)|} \approx \frac{\Gamma(n+1)}{(h_0 k \cos \theta)^n}. \quad (26)$$

The last approximation uses the Bessel function expansion for small arguments<sup>18</sup> and is therefore only valid when the ground displacement amplitude is small in comparison to the ultrasound wave number. We can obtain an estimate of the surface displacement amplitude  $\hat{h}_0$  from the Fourier transform peak magnitude and any of the sidebands,

$$\hat{h}_0 = \frac{1}{k \cos \theta} \left[ \frac{n! |P(\omega' = \omega \pm n\omega_g)|}{|P(\omega' = \omega)|} \right]^{(1/n)}. \quad (27)$$

The corresponding velocity amplitude is obtained from the displacement amplitude  $\hat{v}_g = \omega_g \hat{h}_0$ . The first-order sidebands  $n = \pm 1$  at frequency  $\omega' = \omega \pm \omega_g$  are the most prominent of the sidebands especially in the presence of surface roughness and estimates of surface displacements are usually based upon them.

## B. Coherent interferometry

This is a coherent approach that uses data from both the transmitting and receiving ultrasound transducers. It has the potential to track both the amplitude and phase of the surface displacement. The version described here follows the approach of Ref. 12.

We first multiply the source signal,

$$P_0(t) = Q \cos \omega t, \quad (28)$$

to the received signal to obtain

$$M(t) = P(\mathbf{r}, t) P_0(t) = \Re\left\{\frac{1}{2}QB\mathcal{Z}_N(t)(e^{-i2k_z h(t)} + e^{-i2(\omega t + k_z h(t))})\right\}. \quad (29)$$

The first term is the only term needed for tracking the surface displacement. We next low-pass filter the data to remove the second, higher frequency term in Eq. (29) and obtain

$$M_f(t) = \Re\left\{\frac{1}{2}QB\mathcal{Z}_N(t)e^{-i2k_z h(t)}\right\}. \quad (30)$$

For small surface displacement amplitude compared to the ultrasound wavelength, we can approximate  $e^{-2k_z h(t)} \approx 1 - i2k_z h(t)$ . After removal of the mean or dc component of the filtered data, Eq. (30) simplifies to

$$\overline{M_f(t)} \approx -\Re\{iQB\mathcal{Z}_N(t)k_z h(t)\}. \quad (31)$$

In the absence of time-dependent scattering from the rough surface, the only time-varying quantity in Eq. (30) is  $h(t)$ . The temporal variation of the mean filtered data is therefore directly proportional to the ground displacement. This allows us to track both the amplitude and phase of the ground displacement.

It should be noted that the coherent approach can be applied to analyze ultrasound data reflected from both sinusoidal as well as general broadband ground displacements. For instance, for sinusoidal ground displacement with  $h(t)$  satisfying Eq. (23), an estimate for the surface displacement amplitude is

$$\hat{h}_0 = \frac{1}{2k \cos \theta} \frac{\overline{\mathcal{M}_f(\omega' = \omega_g)}}{|P(\omega' = \omega)| |P_0(\omega' = \omega)|}, \quad (32)$$

where  $\overline{\mathcal{M}_f(\omega')}$ ,  $P(\omega')$ , and  $P_0(\omega')$  are the Fourier transforms of the mean low-pass filtered product signal, the received signal, and the source signal, respectively.

## IV. GENERATING TWO-DIMENSIONAL SPATIAL REALIZATIONS OF THE ROUGH SURFACE

We assume the surface roughness heights follow a Gaussian random process that is locally stationary over the imaged area in the measurement time interval. They can be described by a Gaussian probability distribution function, as discussed in the Appendix. For the simulations in Sec. V, we further assume that the spatial correlation function of the roughness heights at any two horizontal locations  $\boldsymbol{\rho}_t$  and  $\boldsymbol{\rho}_{t'}$  on the surface is also Gaussian and can be expressed as

$$\begin{aligned} \langle \zeta(\boldsymbol{\rho}_t) \zeta(\boldsymbol{\rho}_{t'}) \rangle &= C_{\zeta\zeta}(\boldsymbol{\rho}_t - \boldsymbol{\rho}_{t'}) = C_{\zeta\zeta}(\mathbf{R}) \\ &= \sigma_{\zeta}^2 e^{-(1/2)(X^2/\ell_x^2 + Y^2/\ell_y^2)}, \end{aligned} \quad (33)$$

where  $\mathbf{R} = (X, Y) = \boldsymbol{\rho}_t - \boldsymbol{\rho}_{t'} = (x_t - x_{t'}, y_t - y_{t'})$ ,  $\sigma_{\zeta}$  is the standard deviation of the roughness heights on the surface, and  $\ell_x$  and  $\ell_y$  are the correlation lengths for the roughness heights in the  $x$  and  $y$  directions, respectively. For an isotropic rough surface,  $\ell_x = \ell_y$ . Following Eq. (A4), the two-dimensional (2D) Fourier transform of Eq. (33) yields the corresponding spatial wave number spectrum of the rough surface,

$$G(\boldsymbol{\kappa}) = \pi \sigma_{\zeta}^2 \ell_x \ell_y e^{-(\kappa_x^2 \ell_x^2 + \kappa_y^2 \ell_y^2)/4}. \quad (34)$$

The Gaussian probability distribution function is a good assumption for rough surfaces that are the result of a large number of local cumulative events or processes, and therefore obey Gaussian statistics by the central limit theorem.<sup>19,20</sup>

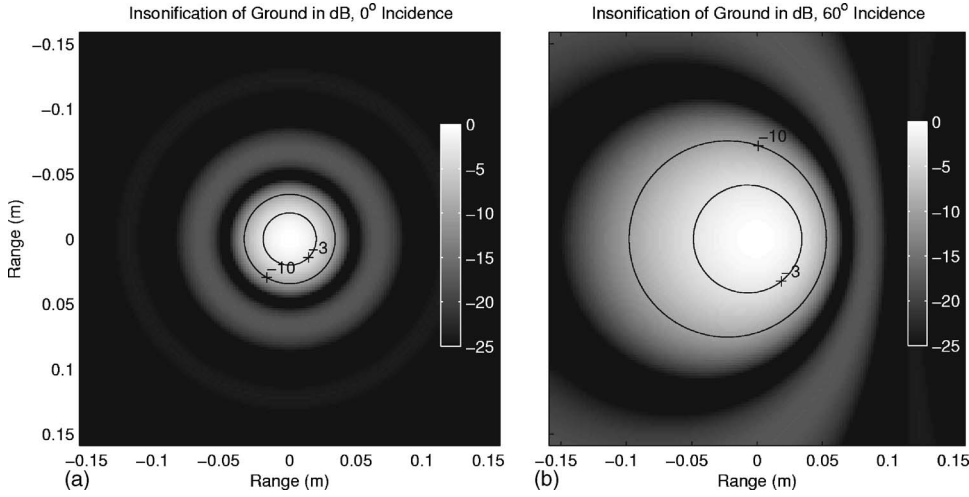


FIG. 2. Magnitude of ultrasound beam pattern in decibels at 50 kHz intercepted by a surface for (a)  $\theta=0^\circ$ , and (b)  $\theta=60^\circ$  incidence of beam axis with surface. The transducer is a circular disk of diameter  $D=3.5$  cm and is positioned 20 cm from the surface. The equivalent beamwidth of the transducer is approximately  $4\lambda/\pi D=14^\circ$ .

Naturally occurring terrain is an example of this.<sup>17</sup> Other correlation functions and related wave number spectra can also be used to characterize the rough surface and the choice depends on the nature of the surface.

Following the approach in Refs. 21 and 17, we describe a procedure for generating spatial realizations of the 2D rough surface with a given wave number spectrum  $G(\boldsymbol{\kappa})$ . Given a rough surface, the 2D Fourier transform of the roughness heights over a finite spatial window with area  $S$  is

$$Z(\boldsymbol{\kappa}) = \int \int_S \zeta(\boldsymbol{\rho}_t) e^{i\boldsymbol{\kappa}\boldsymbol{\rho}_t} dS_t. \quad (35)$$

Here  $Z(\boldsymbol{\kappa})$  is a zero-mean Gaussian random process due to its linear dependence on  $\zeta(\boldsymbol{\rho}_t)$ . According to Parseval's theorem,

$$\sigma_\zeta^2 = \frac{1}{S} \int \int_S \langle |\zeta(\boldsymbol{\rho}_t)|^2 \rangle dS_t = \frac{1}{S} \int \int \langle |Z(\boldsymbol{\kappa})|^2 \rangle \boldsymbol{\kappa} d\boldsymbol{\kappa} d\Theta. \quad (36)$$

From Eq. (A5),  $\sigma_\zeta^2 = C_{\zeta\zeta}(0)$ , so that

$$\langle |Z(\boldsymbol{\kappa})|^2 \rangle = \frac{S}{(2\pi)^2} \langle G(\boldsymbol{\kappa}) \rangle. \quad (37)$$

As  $S$  becomes arbitrarily large, delta-function correlation is achieved across the wave vector domain,

$$\langle Z(\boldsymbol{\kappa})Z(\boldsymbol{\kappa}') \rangle \approx \frac{G(\boldsymbol{\kappa})}{(2\pi)^2} \delta(\boldsymbol{\kappa} - \boldsymbol{\kappa}'),$$

indicating that components of  $Z(\boldsymbol{\kappa})$  with wave vector separations exceeding  $(2\pi)^2/S$  are uncorrelated. A random realization of the rough surface height  $\zeta(\boldsymbol{\rho}_t)$  can be obtained as the inverse Fourier transform of  $Z(\boldsymbol{\kappa})$  under the assumption that  $Z(\boldsymbol{\kappa})$  are zero-mean Gaussian random variables that are uncorrelated when sampled at wave vector intervals of at least  $(2\pi)^2/S$  and have variance  $\langle G(\boldsymbol{\kappa}) \rangle S / (2\pi)^2$ .

For the numerical simulation in Sec. V, we create the 2D rough surfaces by first generating the real and imaginary parts of a 2D matrix of complex Gaussian random variables

with zero mean and variance  $\langle G(\boldsymbol{\kappa}) \rangle S / (2\pi)^2$ . This matrix corresponds to  $Z(\boldsymbol{\kappa})$ . We apply the symmetry property of Fourier transforms of real signals to ensure that  $Z(\boldsymbol{\kappa}) = Z(-\boldsymbol{\kappa})^*$ . We then take the inverse Fourier transform of  $Z(\boldsymbol{\kappa})$  to yield a purely real 2D rough surface with the required statistical property.

## V. NUMERICAL SIMULATION

Here we investigate the performance of the ultrasound vibrometer for measuring surface displacement while continuously scanning a sinusoidally oscillating randomly rough ground. The performance of the system is investigated as a function of the ultrasound frequency, angle of incidence of the ultrasound beam, system scan velocity, and stand-off distance of the transducers from the surface. The stand-off distance determines the area of ground insonified by the system. We simulate different surface types, such as those of sand and gravel, by varying the roughness height standard deviation and correlation length scale of the surface. The performance of the system is quantified by examining the accuracy of the displacement estimation using both the coherent and incoherent data analysis schemes. In the examples to follow, the ultrasound source frequency is  $f=50$  kHz, unless otherwise stated. The ground is assumed to be oscillating harmonically at a frequency of 120 Hz with a displacement amplitude of  $h_0=2.5$   $\mu\text{m}$ .

The transducer is modeled as a baffled circular disk of diameter  $D=3.5$  cm. The equivalent beamwidth of the main lobe of the transducer is  $\theta_e=4\lambda/\pi D=14^\circ$  and the far field for the transducer begins at  $D^2/\lambda=18$  cm. The transducer is originally positioned at a distance of  $r_0=r=20$  cm from the ground. The theoretical beam pattern is calculated based on the transducer dimensions. Figures 2(a) and 2(b) show the beam-pattern amplitude  $w(\boldsymbol{\rho}_t)$  projected onto the ground for two different scenarios where the transducer main lobe axis makes the angle  $\theta=0^\circ$  and  $\theta=60^\circ$ , respectively, with the surface normal. We observe that the dominant region of the surface insonified by the transducer is small, with a width of about  $\rho_e=r\theta_e=4.9$  cm for  $0^\circ$  incidence. For  $60^\circ$  incidence, the beam pattern on the ground is asymmetric about the  $y$  axis and the dominant region insonified has a width of

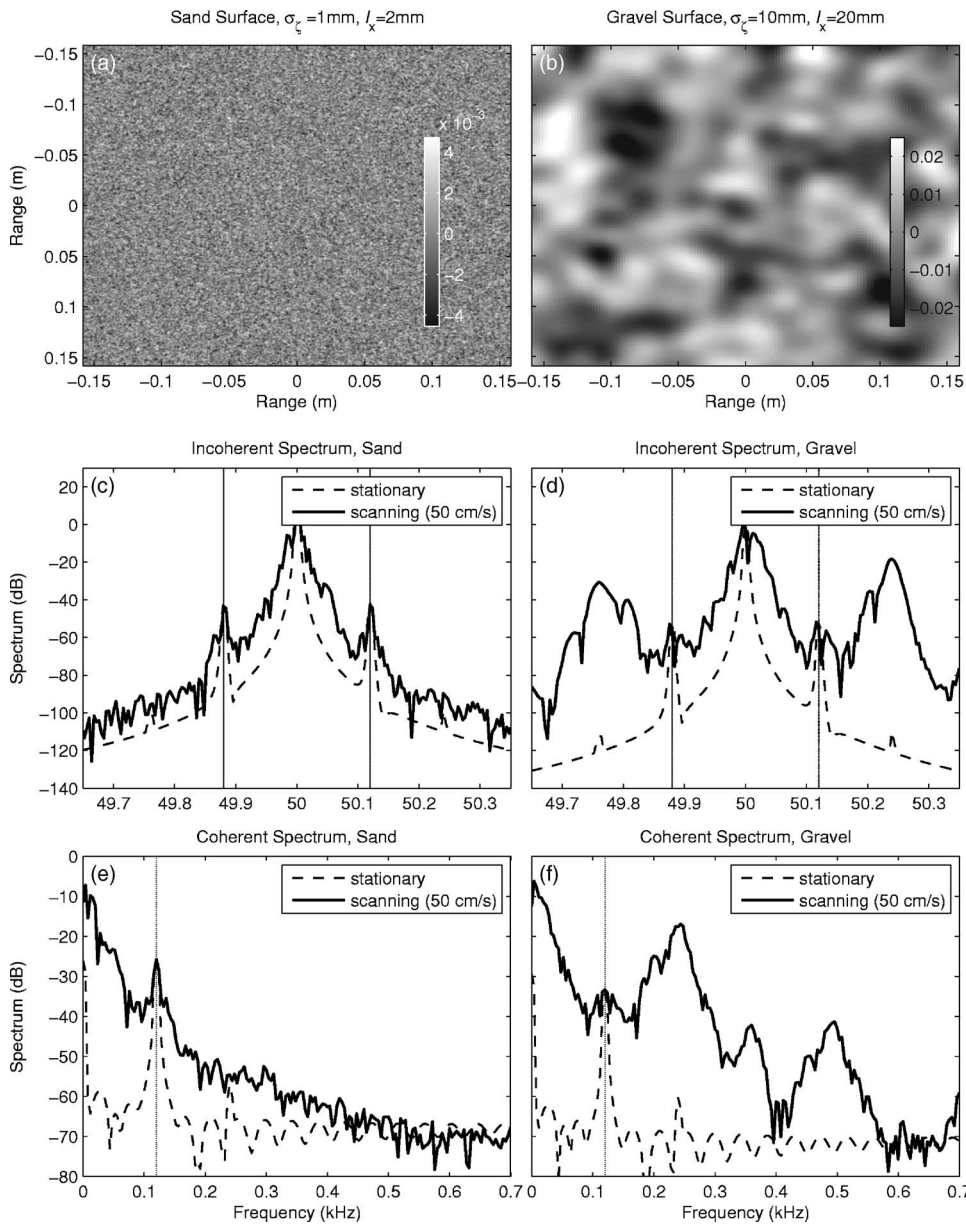


FIG. 3. Realizations of randomly rough (a) medium sand and (b) gravel surfaces. Spectrum of received ultrasound field,  $10 \log_{10} |\mathcal{P}(\omega')|^2$ , reflected and scattered off harmonically oscillating (c) medium sand and (d) gravel surfaces for an ultrasound vibrometer continuously scanning the surface at a speed of 50 cm/s. The corresponding results for the stationary vibrometer are plotted for comparison. (e) Medium sand and (f) gravel are the corresponding coherently processed spectrum of low-pass filtered mixed signal,  $10 \log_{10} |\mathcal{M}_f(\omega')|$ . The spectra are plotted for an ultrasound source level of 0 dB re 20  $\mu$ Pa at 1 m ( $f=50$  kHz,  $f_g=120$  Hz,  $h_0=2.5$   $\mu$ m,  $\theta=0^\circ$ ,  $z=z_0=0.2$  m,  $T=0.25$  s).

roughly  $\rho_c/\cos \theta_c=9.8$  cm. The ground vibration wavelength at the acoustic excitation frequency of 120 Hz is roughly 2 m. This is much larger than the resolution footprint of the ultrasound system making lateral variations in ground vibration negligible in the measurement. Since the material density of the ground is much larger than in air, the reflection coefficient can be approximated as a constant,  $R \approx 1$  from Eq. (9). In all the examples to follow, the results are plotted for a ultrasound system with source level of 0 dB re 20  $\mu$ Pa at 1 m.

### A. Performance of scanning ultrasound vibrometer for varying surface types

In this section, the performance of the ultrasound vibrometer is studied as a function of roughness height standard deviation and correlation length scale of the rough surface. Figures 3(a) and 3(b) show realizations of isotropic rough surfaces for medium sand and gravel environments, respectively. The surface roughness is assumed to follow a Gauss-

ian random process with Gaussian correlation function as described in Sec. IV. The roughness height standard deviation and correlation length scales for medium sand are  $\sigma_h=1$  mm,  $\ell_x=2$  mm, and those for gravel are  $\sigma_h=10$  mm,  $\ell_x=20$  mm. Relative to the ultrasound wavelength of  $\lambda=6.8$  mm, the sand surface is considered to be moderately rough with  $k\sigma_z=0.9$ , while the gravel surface is considered to be very rough with  $k\sigma_z=9.2$ .

Figures 3(c) and 3(d) plot the Fourier spectrum,  $20 \log_{10} |\mathcal{P}(\omega')|$ , of the received ultrasound field reflected and scattered off the oscillating rough surface for the sand and gravel environments, respectively. The received field is computed using Eq. (15) and a Hanning window was applied to the simulated data in time before calculating the spectrum. The results are plotted for the stationary ultrasound vibrometer as well as the vibrometer system continuously scanning the ground at a speed of  $v_u=50$  cm/s. For the stationary vibrometer in both environments, we observe a peak in the spectrum at 50 kHz corresponding to the original ultrasound

transmitted frequency. We also observe the prominent first-order sidebands at 49.88 and 50.12 kHz which are Doppler shifts  $f \pm f_g$  in the reflected signal caused by the harmonically oscillating ground. The second-order sidebands are also visible, but they have much smaller amplitudes. For the continuously scanning vibrometer, the spectrum of the received signal is degraded due to scattering from the rough surface. This degradation is small for the sand surface, but is significant for the gravel surface.

Incoherent signal analysis for the ground displacement amplitude is obtained from the ratio of the spectral peak to the first-order sidebands following Eq. (27). For the continuously scanning ultrasound vibrometer, we obtain  $\hat{h}_0 \approx 2.46 \mu\text{m}$  for the medium sand surface,  $\hat{h}_0 \approx 3.7 \mu\text{m}$  for the gravel surface. This corresponds to accuracies of 98% and 52% for the sand and gravel surfaces, respectively, with incoherent processing. These estimates are based on a single realization of the surface. The results after averaging over multiple realizations will be discussed in the next section.

Figures 3(e) and 3(f) show the Fourier spectrum of the filtered mix signal,  $10 \log_{10} |M_f(\omega')|$ , after removal of the mean and application of a Hanning window in time to the mix signal in the sand and gravel environments, respectively. The results are again plotted for both the stationary vibrometer and the vibrometer continuously scanning the ground at 50 cm/s. A prominent peak in the spectrum is observed in the sand and gravel environments at the ground oscillation frequency of 120 Hz when the vibrometer is stationary. For the continuously scanning system, the spectrum is randomized significantly in the gravel environment and no distinct peak can be observed at the desired frequency. Coherent signal analysis for the ground displacement amplitude is obtained by application of Eq. (32). For the continuously scanning vibrometer, we estimate  $\hat{h}_0 \approx 2.8 \mu\text{m}$  for sand and  $\hat{h}_0 \approx 1.79 \mu\text{m}$  for gravel. Corresponding accuracies are 89% and 72% for the sand and gravel surfaces, respectively, with coherent processing for a single realization of the surface.

The above-presented analysis indicates that when the vibrometer is stationary while acquiring data, it is expected to perform well in estimating surface displacement regardless of the rough surface condition. This is because random scattering from the rough surface is constant and does not add time-dependent noise to the measurement when the vibrometer is stationary. Since the sidebands for the stationary measurement stand above the background spectrum level by over 40 dB, in the absence of other sources of noise, the system is sensitive to displacements on the order of 0.1 nm. For the continuously scanning system, the 50 kHz vibrometer is expected to perform well in estimating surface displacements for sandy and other less rough surfaces at relatively high scan speeds. The performance of the 50 kHz vibrometer is degraded for gravel and other surfaces that are more rough indicating that these surfaces should not be continuously scanned at high speeds. In Sec. V D, we determine the limiting scan speeds for gravel and sandy environments for an ultrasound vibrometer to be used in acoustic landmine confirmation sensing.

## B. Random spectral broadening in the continuously scanning vibrometer

Here we analyze the randomization in the spectrum that is caused by scattering from a randomly rough surface for the scanning ultrasound vibrometer. Figure 4(a) shows the spectrum of the received signal for a stationary ultrasound vibrometer reflected from a nonoscillating smooth surface. Nearly the same spectrum is obtained for the continuously scanning vibrometer over the same surface. Both systems measure the signal reflected from the smooth surface which has a peak in the spectrum at the ultrasound frequency of 50 kHz. For a smooth surface that is oscillating sinusoidally, Fig. 4(b) shows the introduction of sidebands at  $f \pm n f_g$  to the spectrum of the received field for both the stationary and scanning systems. Here the sidebands up to  $n=2$  are visible. When the surface becomes rough but is nonoscillating, the received signal differs for the stationary and continuously scanning ultrasound systems. For the stationary system, the received signal spectral peak at 50 kHz is reduced in amplitude due to nonspecular scattering of the field into other directions away from the receiving transducer as shown in Fig. 4(c). For the scanning system, Fig. 4(e), in addition to a reduction of the magnitude, there is also random broadening of the spectral peak. This spectral broadening around the peak is due to Doppler shifts caused by undulations on the rough surface as the transducer moves either toward or away from the roughness elements. When the rough surface oscillates harmonically, the effects noted for the nonoscillating rough surface now become applicable to both the spectral peak and sidebands for the harmonically oscillating rough surface. As shown in Fig. 4(d), for the stationary vibrometer, the level of both the peak and sidebands have been reduced due to scattering from the oscillating rough surface. In continuous scan mode, Fig. 4(f), the spectrum of the received field broadens for both the peak and sidebands in comparison to the stationary case.

The Doppler broadening of the spectrum is random and dependent on the particular realization of the rough surface. This can be noted in Figs. 5(a) and 5(b), which show the received signal spectrum obtained for the vibrometer with scan velocity of 50 cm/s for ten independent realizations of the sand and gravel surfaces, respectively. The average spectrum in Fig. 5 is found by incoherently averaging intensity of the individual spectra. When it is possible for the vibrometer to make several independent measurements of the surface in a given location, the estimation of surface displacement and accuracy can be improved. This would occur, for instance, when the vibrometer makes multiple passes in varying directions over a given location so that the scans can be approximated as independent. For the ten independent realizations of the surface shown in Fig. 5, there are two possible approaches for estimating  $h_0$ . We can either estimate  $h_0$  for each independent realization and then calculate the average, or estimate  $h_0$  from the single averaged spectrum. In the former approach, we calculate the percentage root-mean-square (rms) error,  $e$ , for surface displacement estimation using

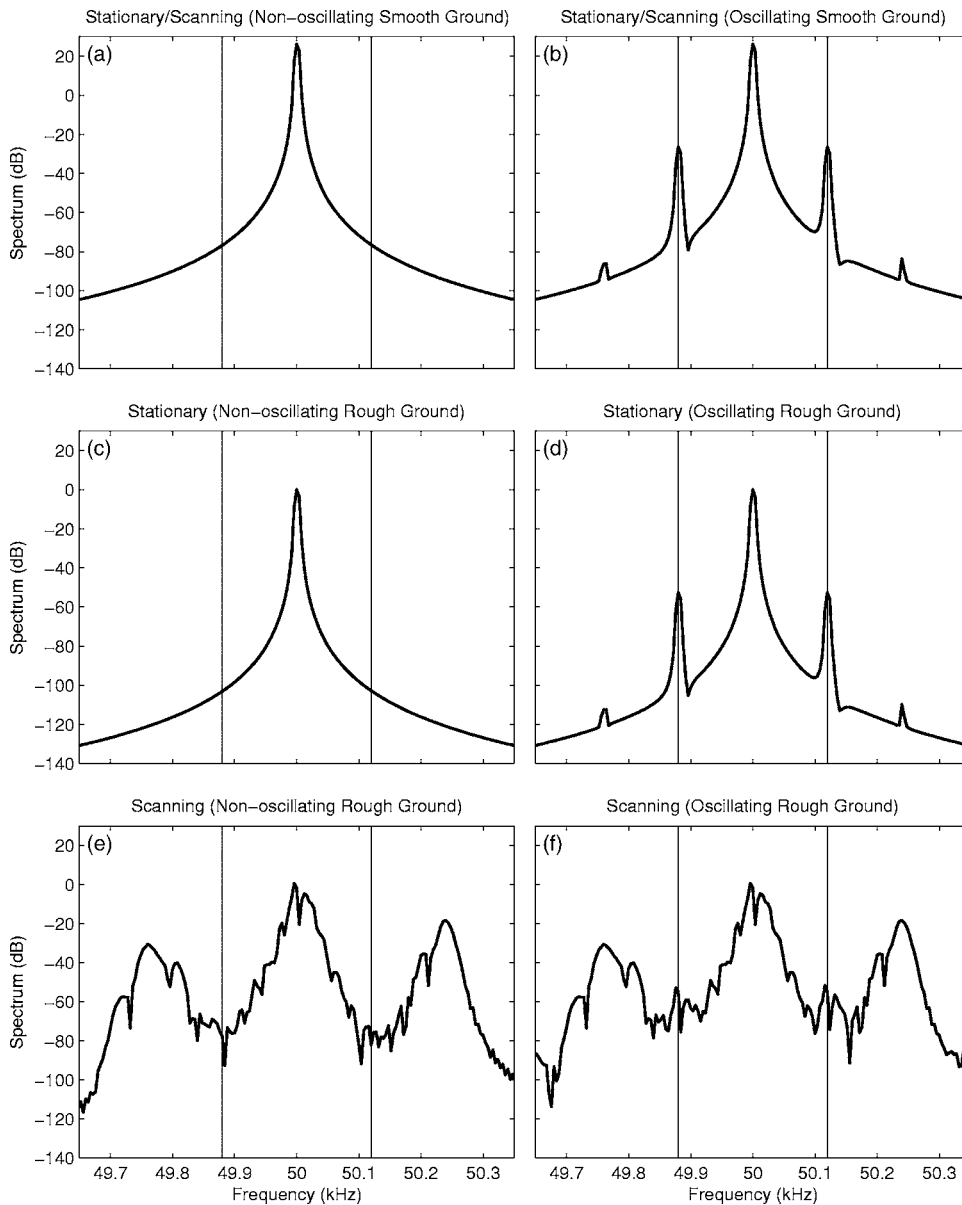


FIG. 4. Spectrum of ultrasound field at 50 kHz reflected and scattered at normal incidence off a (a) smooth and nonoscillating surface for the stationary vibrometer (same result for scanning system), (b) smooth and harmonically oscillating surface for stationary vibrometer (same result for scanning system), (c) nonoscillating rough gravel surface with stationary vibrometer, (d) oscillating rough gravel surface with stationary vibrometer, (e) nonoscillating rough gravel surface with scanning vibrometer, and (f) harmonically oscillating rough gravel surface with scanning vibrometer. In (a), (b), (e), and (f) the scanning vibrometer is moving at 50 cm/s. Unless otherwise specified, the sonar, measurement, and surface parameters are the same as in Fig. 3(d).

$$e = \frac{\sqrt{\langle (\hat{h}_0 - h_0)^2 \rangle}}{h_0} 100\% . \quad (38)$$

The results are summarized in Table I. The analysis indicates that surface displacement amplitude can be estimated with

higher accuracy and smaller standard deviation for sand surfaces than gravel with a vibrometer scan speed of 50 cm/s. Furthermore, averaging the results from multiple independent scans helps reduce the error in the displacement estimation, as expected.

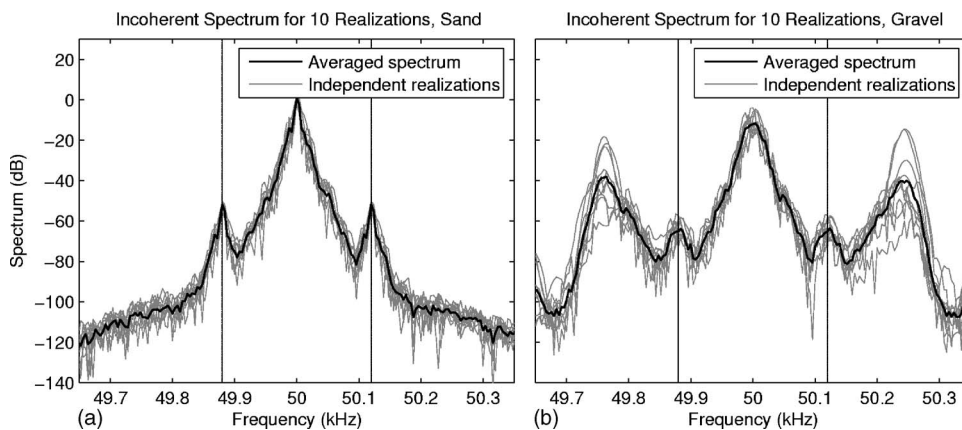


FIG. 5. Spectrum of received ultrasound field reflected and scattered off an oscillating (a) medium sand and (b) gravel surfaces. Results were for ten independent realizations of the sand and gravel surfaces, respectively. The average spectrum is obtained by incoherently averaging the intensity of the individual spectra. The ultrasound scan speed is 50 cm/s. Unless otherwise specified, the sonar, measurement, and surface parameters are the same as in Figs. 3(c) and 3(d), respectively.

TABLE I. Estimates of surface displacement amplitude from incoherent processing for a 50 kHz ultrasound vibrometer continuously scanning the surface at a speed of 50 cm/s. The estimates are obtained by either using data from a single scan, averaging  $h_0$  estimates over ten independent scans at a given location, or estimating  $h_0$  from the average spectrum for ten independent realizations. The quantities in parentheses are the accuracies for the estimation.

	Single realization	Averaged estimates from ten realizations	Averaged spectrum
Sand	2.46 (98%)	2.50 (99.8%, 0.7% rms error)	2.50 (99.8%)
Gravel	3.7 (52%)	2.55 (98%, 10% rms error)	2.68 (93%)

The time domain reflected signal from the harmonically oscillating sand and gravel surface is shown in Fig. 6 for the continuously scanning vibrometer at 50 cm/s speed. We observe time-dependent fluctuations in signal amplitude caused by interference of randomly scattered fields from the random rough surface, with severe fade-outs for the gravel surface at specific time instances. It should be noted that for the stationary vibrometer, scattering from the rough surface does not lead to time-dependent variations in the reflected signal amplitude. The statistical distribution for the amplitude and phase of the scattered ultrasound field is discussed in Ref. 19 and 26.

### C. Effect of ultrasound frequency, measurement time, insonification area, angle of incidence, and scanning speed

Here we investigate the vibrometer system design and measurement parameters that can be adjusted to enhance the measurement of surface displacement for very rough surfaces, like that of gravel. Figure 7 compares the effect of lowering or raising the ultrasound source frequency from 50 kHz for the gravel surface. The spectral peak and sidebands of the received ultrasound signal are more pronounced at 20 kHz. There is less Doppler broadening of the signal spectrum because of reduced scattering from the rough surface with the longer ultrasound wavelength at 20 kHz,  $k\sigma_\zeta = 3.7$ , and the surface appears smoother. The spectrum worsens at 100 kHz when the ultrasound wavelength shortens leading to more significant scattering from the rough surface,  $k\sigma_\zeta = 18.4$ .

The effect of adjusting the measurement time or length of signal used in computing the signal spectrum is illustrated in Fig. 8(a) for the gravel surface. The measurement time change does not lead to significant changes in the signal spectrum. It should be noted that the measurement time  $T$

along with the scan speed  $v_u$  determine the range resolution  $\Delta x$  of the vibrometer,  $\Delta x = Tv_u$ . For example, small antipersonnel mines require a smaller range resolution in comparison to larger antitank mines. Furthermore, inverse of the measurement time also determines the frequency resolution of the signal spectrum,  $\Delta f = 1/T$ . The frequency resolution should be set to clearly resolve the frequency sidebands due to ground oscillation and the ultrasound peak frequency. The frequency resolution and range resolution requirements then set a limit on the maximum scan speed such that  $v_u \leq \Delta x \Delta f$ .

Adjusting the distance of the ultrasound vibrometer system from the ground determines the area of ground insonified, and effects the spectrum of the received signal as shown in Fig. 8(b). Increasing the area of ground insonified improves the signal-to-noise ratio (SNR) of the sidebands slightly as more roughness elements are imaged, which statistically reduces the scattering noise level. Increasing the angle of incidence appears to have a more prominent effect on enhancing the signal spectrum. As illustrated in Fig. 8(c), the SNR for the sidebands improves when the grazing angle is increased from  $0^\circ$  to  $60^\circ$  incidence. The ultrasound wavelength projected onto the rough surface is larger at  $60^\circ$  incidence leading to reduced scattering from the rough surface since  $k_z \sigma_\zeta = k \cos \theta \sigma_\zeta = 4.6$ .

The most sensitive parameter for the scanning vibrometer is its scan velocity,  $v_u$ . We illustrate the effect of raising and lowering scan speeds on the received signal spectrum for sand and gravel in Figs. 9(a) and 9(b), respectively. The spectra shown were incoherently averaged over ten realizations of the rough surface types. When the scan speed is reduced from 1 m/s to 50 cm/s or 20 cm/s, the SNR for both the peak and sidebands are tremendously enhanced in sand and moderately in gravel. In the limit where the vibrometer becomes stationary, in comparison with Figs. 4(c) and

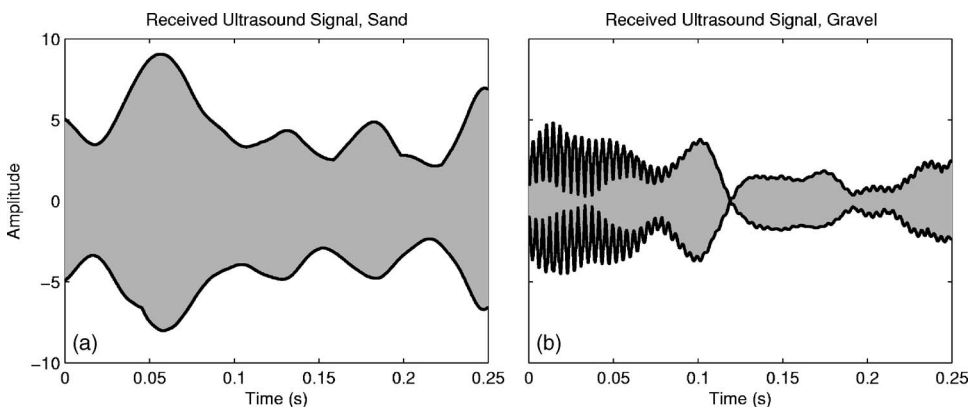


FIG. 6. Time domain wave form of ultrasound received field reflected and scattered off harmonically oscillating (a) sand and (b) gravel surface for the continuously scanning vibrometer. These were used to compute the spectra shown in Figs. 3(c) and 3(d) for the continuously scanning system.

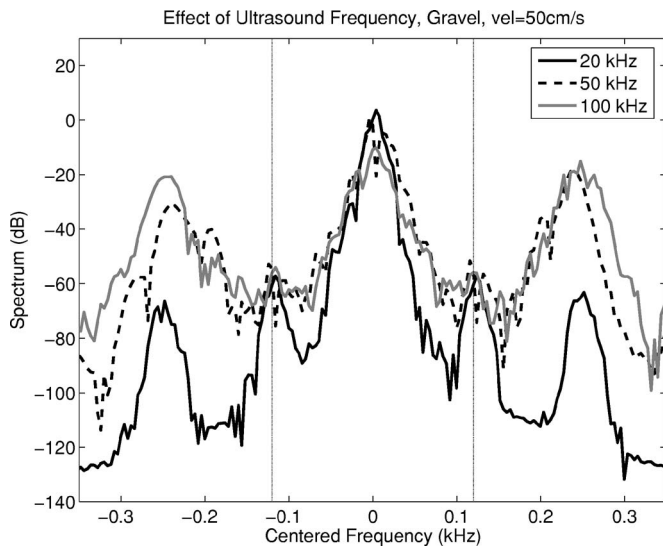


FIG. 7. Effect of adjusting the ultrasound source frequency on the spectrum of the received signal. The measurement setup is the same as in Fig. 3(d). The  $x$  axis should be scaled according to the ultrasound frequency for each of the cases.

4(d), the performance of the vibrometer is significantly improved. In Fig. 9(b) for gravel, we observe periodic local peaks in the spectrum in addition to the peak at the ultrasound frequency and sidebands at  $f \pm n f_g$  due to ground oscillation. These additional periodic peaks are caused by Doppler shifts in the ultrasound frequency arising from motion of the vibrometer over the rough surface. As the surface height changes, it leads to frequency variations in the reflected ultrasound signal for the scanning vibrometer that is independent of ground oscillations, as can be seen by comparing

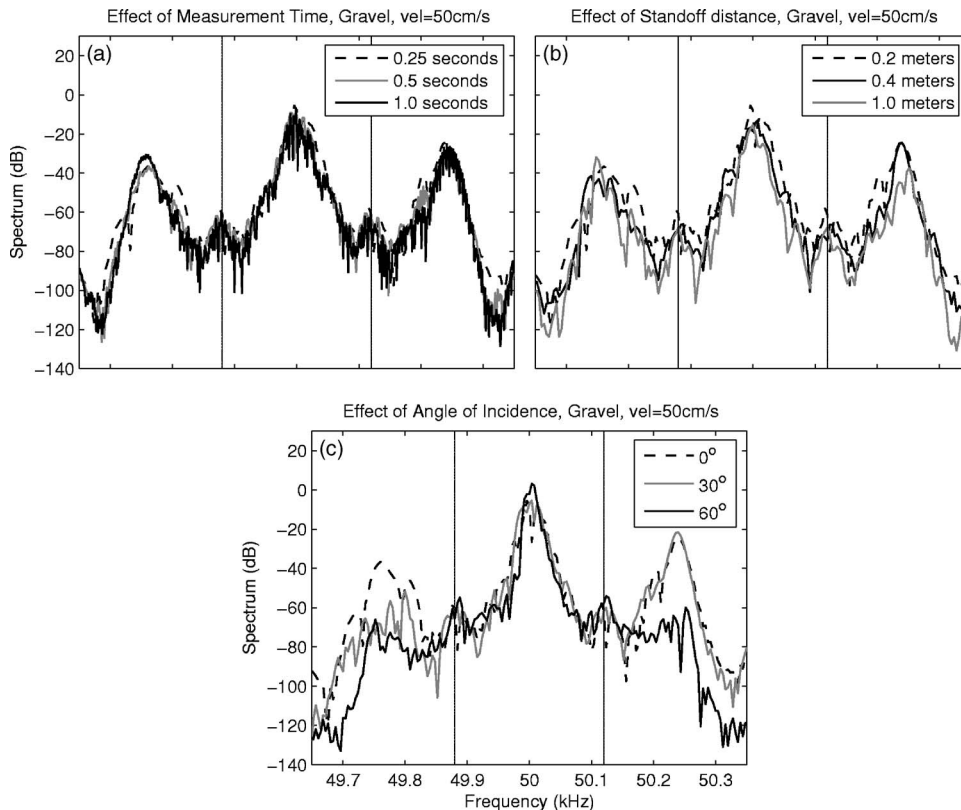


FIG. 8. Effect of adjusting the (a) measurement time  $T$ , (b) vibrometer stand-off distance  $z$ , and (c) angle of incidence  $\theta$ , on the spectrum of the received signal. Unless otherwise specified, the measurement setup is the same as Fig. 3(d).

Figs. 4(e) and 4(f). Our analysis shows that their spacing in the frequency spectrum is directly proportional to the scan velocity and inversely proportional to the correlation length scale of the rough surface,  $v_u/\ell_x$ . This factor determines the number of undulations on the rough surface traversed by the vibrometer per unit time. The amplitude of these periodic peaks depends on the surface gradient. For the sand surface, the roughness heights are not large enough to cause any significant Doppler shift of the ultrasound beam and so these additional peaks do not appear within the bandwidth illustrated in Fig. 9(a).

In an experimental scenario, when the periodic peaks due to rough surface scattering occur at the sidebands due to ground oscillation, one should alter the vibrometer scan speed or the frequency of ground oscillation so that the peaks due to rough surface scattering are moved out of the frequency sidebands of interest.

#### D. Limiting scan speed for acoustic landmine imaging

Here we investigate limiting scan speeds for an ultrasound vibrometer deployed as part of an acoustic landmine confirmation sensor over natural terrain. The ground surface oscillation amplitudes at the mine resonance frequency in areas containing mines are dependent on the type of mine, whether it is an antipersonnel mine or a larger antitank mine, burial depth of the mine, and the intensity with which the ground is excited at the low acoustic or seismic frequencies. For shallow buried mines, the ground is typically incident with acoustic field intensities that lead to surface velocity amplitudes of 40–500  $\mu\text{m/s}$  over areas enclosing mines at the mine resonance frequencies, and velocity amplitudes of

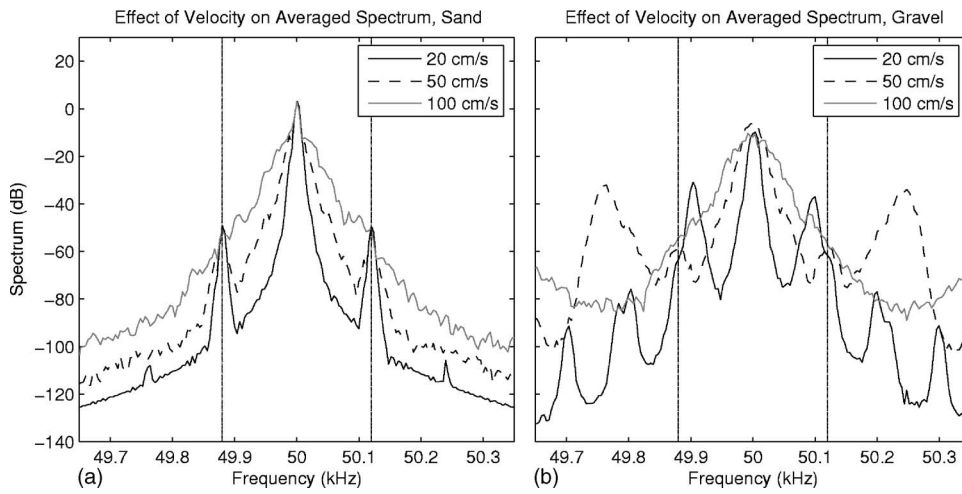


FIG. 9. Effect of adjusting the vibrometer scan velocity on the incoherently averaged spectrum of received signal from (a) sand and (b) gravel surfaces. All other parameters are the same as in Figs. 5(a) and 5(b).

roughly  $20\text{--}50\ \mu\text{m/s}$  in areas devoid of mines.<sup>5,10</sup> In order for the ultrasound system to clearly image a mine, it must distinguish surface velocity amplitudes in areas covering a mine from an area devoid of mines. The scattering noise floor level should not mask the Doppler shifted sideband levels caused by surface oscillation in the received signal spectrum. From all the spectra shown so far, we observe that the scattering noise floor level in the signal spectrum is a function of frequency. Here we illustrate results that are applicable to mine resonance frequencies of  $f_g=140\ \text{Hz}$  and  $f_g=400\ \text{Hz}$ , which are the resonance frequencies typically observed and used for imaging mines of interest.<sup>5,10</sup> For  $f_g=140\ \text{Hz}$ , the corresponding surface displacement amplitudes in areas that enclose a mine span from  $0.05$  to  $0.5\ \mu\text{m}$ , while at  $f_g=400\ \text{Hz}$ , the displacement amplitudes span from  $0.02$  to  $0.16\ \mu\text{m}$ .

In Figs. 10(a) and 10(b) we plot the scattering noise floor level measured by the received ultrasound transducer, as a function of scan speed for the sand and gravel surfaces, respectively, for a  $50\ \text{kHz}$  ultrasound vibrometer at Doppler shift frequencies of  $f_u \pm f_g$  for  $f_g=140$  and  $f_g=400\ \text{Hz}$ . The

scattering noise floor levels were converted to equivalent displacement amplitudes using Eq. (27). In the sand environment, the curves were generated by first simulating the averaged spectrum for ten independent realizations of the rough surface for different ultrasound scan speeds from  $20$  to  $160\ \text{cm/s}$ . The corresponding noise floors at the required sideband frequencies were extracted and are shown as asterisks in the plot. We then fit a quadratic model to these points and the best fit curve is shown as a solid line. For the gravel environment, we first ignored the periodic Doppler shifted peaks due to significant rough surface scattering by interpolating the noise floor levels at frequencies outside of these periodic peaks. These noise floor levels are shown as asterisks with the corresponding quadratic curve fit. We did this because the frequency occurrence of the periodic peaks is a function of scan velocity and they do not occur continuously at a given sideband frequency of interest as scan velocity is varied. However, for the two resonance frequencies of interest, we indicate using circles the level of the periodic Doppler shifted peaks when they occur at the sidebands of

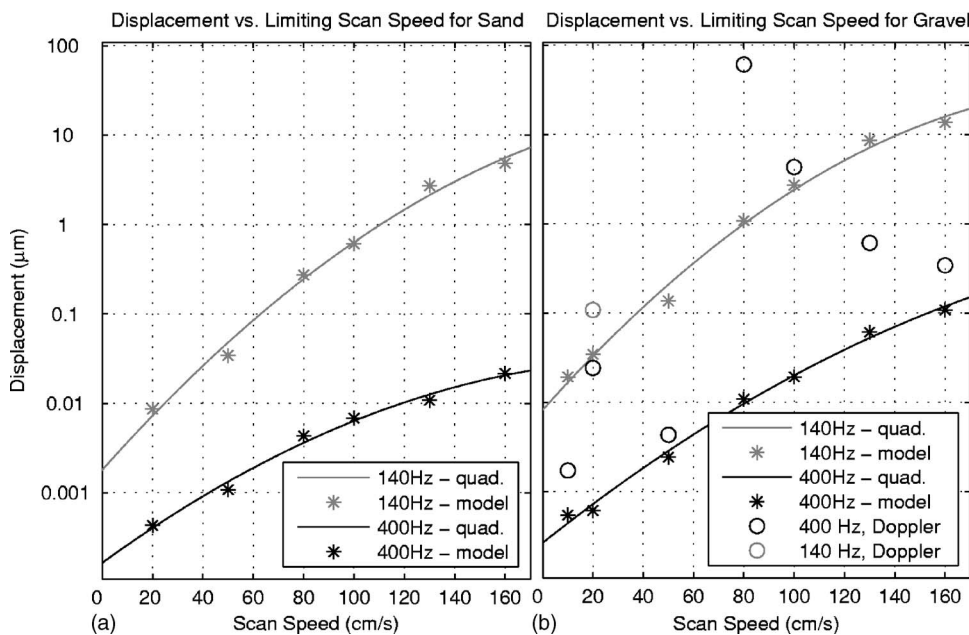


FIG. 10. Averaged spectrum of scattered noise level vs scan speed in (a) sand and (b) gravel for sidebands corresponding to ground resonance frequencies of  $140$  and  $400\ \text{Hz}$  for a  $50\ \text{kHz}$  ultrasound vibrometer. The scattered noise level is converted to equivalent displacement amplitude using Eq. (27).

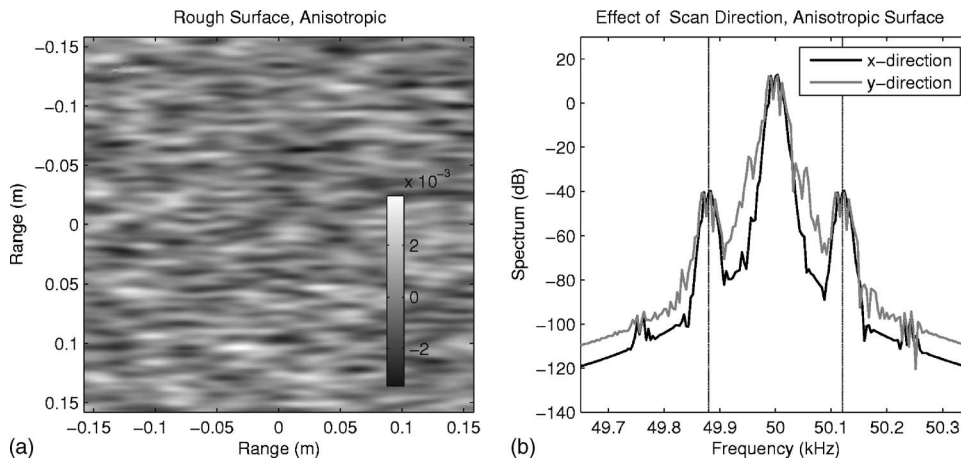


FIG. 11. (a) Anisotropic rough surface with five times longer correlation length in the  $x$  direction than in the  $y$  direction. (b) Similar to Fig. 3(d) but for the vibrometer continuously scanning in the  $x$  direction or  $y$  direction at 50 cm/s.

interest. These periodic Doppler shifted peaks are not present at the sidebands of interest for the sand surfaces.

We observe from Figs. 10(a) and 10(b) that the noise floor increases with scan speed as expected in both the sand and gravel environments. For the sand surface, the increase is monotonic at the mine resonance frequencies of interest. The limiting scan speed in sand is around 50 cm/s for the 140 Hz resonance frequency and 150 cm/s for the 400 Hz resonance. At scan speeds higher than this, the scattering noise floor is expected to mask the sidebands due to ground oscillation in the received signal spectrum. In the gravel environment, the increase is nonmonotonic due to the appearance of periodic peaks in the signal spectrum arising from Doppler shifts of the ultrasound frequency from rough surface scattering. The scan speeds are then limited to 20 cm/s at 140 Hz resonance and 60 cm/s for 400 Hz resonance. The limiting scan speeds may be further improved for the ultrasound system by lowering the ultrasound frequency. In addition to speckle noise, the vibrometer scan speed may also be limited by the range and frequency resolution requirement of the system as discussed in Sec. V C.

We should point out that the noise floor analysis in Ref. 10, Fig. 10, for the laser vibrometer was done experimentally with the laser scanning over a sheet of *paper*. It therefore cannot be compared to the noise floor analysis done here for the ultrasound vibrometer over natural terrain. The limiting scan speeds for the ultrasound vibrometer over the sand and gravel surfaces derived here should be much higher than that for a laser vibrometer over these same surfaces since the laser wavelength is a thousand times smaller than the ultrasound wavelength.

### E. Anisotropic rough surfaces

For an anisotropic rough surface, such as sediment ripples formed by wind blowing in a specific direction over the surface, the performance of the vibrometer is dependent on the scan direction of the system. Figure 11(a) shows an anisotropic rough surface with a correlation length of 10 mm in the  $x$  direction and a smaller correlation length of 2 mm in the  $y$  direction. The roughness height standard deviation for this rough surface is 1 mm. We observe better performance for the ultrasound system when scanning in the direction with the larger correlation length. This is expected since the

rough surface gradients are much smaller in the  $x$  direction and therefore the spectral broadening due to Doppler, which is dependent on surface slope, is less significant.

## VI. CONCLUSION

An analytic model for the ultrasound field reflected off a vibrating rough surface has been developed from Green's theorem for a scanning ultrasound vibrometer system. The model is bistatic and incorporates the beam patterns of both the transmitting and receiving ultrasound transducers, as well as the statistical properties of the rough surface. The ultrasound data from this model is then analyzed using two different processing schemes, coherent interferometry and incoherent Doppler shift spectra, to yield estimates of surface displacement amplitude for a sinusoidally oscillating rough surface. The model is applied to determine sonar design parameters and measurement geometry that can enhance performance of the scanning ultrasound vibrometer measuring ground displacements from acoustic/seismic excitation in acoustic landmine detection. Simulations with the model indicate that performance of the vibrometer is highly dependent on scan velocity, and vibrometer frequency, as well as statistical properties of the rough surface. The model has been applied to determine limiting scan speeds for an ultrasound vibrometer used for acoustic landmine imaging in natural terrain environments.

## APPENDIX: STATISTICAL DESCRIPTION OF ROUGH SURFACE

Here we provide a statistical description of the randomly rough surface in terms of its probability distribution, correlation function, and spectrum of roughness heights following the approach of Refs. 21 and 17. We assume that the height  $\zeta(\boldsymbol{\rho}_t)$  of the rough surface boundary at horizontal location  $\boldsymbol{\rho}_t$  follows a Gaussian random process in space with mean  $\langle \zeta \rangle = 0$ , and variance  $\sigma_\zeta^2 = \langle \zeta^2 \rangle - \langle \zeta \rangle^2$ . The probability density function of the rough surface height is

$$p_\zeta(\zeta) = \frac{1}{\sqrt{2\pi}\sigma_\zeta} \exp\left(-\frac{(\zeta - \langle \zeta \rangle)^2}{2\sigma_\zeta^2}\right). \quad (\text{A1})$$

The joint probability density function of the roughness height at horizontal locations  $\boldsymbol{\rho}_t$  and  $\boldsymbol{\rho}_{t'}$  can be expressed as

$$p(\zeta(\mathbf{r}_t), \zeta(\mathbf{r}_{t'})) = \frac{1}{2\pi\sigma_{\zeta(\mathbf{r}_t)}\sigma_{\zeta(\mathbf{r}_{t'})}(1-\varrho^2)^{1/2}} \exp\left(-\frac{[(\zeta^2(\mathbf{r}_t)\sigma_{\zeta(\mathbf{r}_{t'})}^2 - 2\zeta(\mathbf{r}_t)\zeta(\mathbf{r}_{t'})\varrho\sigma_{\zeta(\mathbf{r}_t)}\sigma_{\zeta(\mathbf{r}_{t'})} + \zeta^2(\mathbf{r}_{t'})\sigma_{\zeta(\mathbf{r}_t)}^2)]}{2\sigma_{\zeta(\mathbf{r}_t)}^2\sigma_{\zeta(\mathbf{r}_{t'})}^2(1-\varrho^2)}\right), \quad (\text{A2})$$

where  $\varrho$  is the correlation coefficient defined as

$$\varrho = \frac{\langle \zeta(\mathbf{r}_t)\zeta(\mathbf{r}_{t'}) \rangle - \langle \zeta(\mathbf{r}_t) \rangle \langle \zeta(\mathbf{r}_{t'}) \rangle}{\sqrt{(\langle \zeta(\mathbf{r}_t) \rangle^2 - \langle \zeta(\mathbf{r}_t) \rangle^2)(\langle \zeta(\mathbf{r}_{t'}) \rangle^2 - \langle \zeta(\mathbf{r}_{t'}) \rangle^2)}}. \quad (\text{A3})$$

We assume that the roughness heights follow a locally stationary random process within the area imaged by the system for each measurement time interval. Its correlation function can then be expressed as a Fourier transform of its wave number spectrum  $\mathcal{G}(\boldsymbol{\kappa})$  following<sup>22</sup>

$$\begin{aligned} \langle \zeta(\mathbf{r}_t)\zeta(\mathbf{r}_{t'}) \rangle &= C_{\zeta\zeta}(\mathbf{r}_t - \mathbf{r}_{t'}) \\ &= \frac{1}{(2\pi)^2} \int_0^{2\pi} \int_0^\infty \mathcal{G}(\boldsymbol{\kappa}) e^{i\boldsymbol{\kappa} \cdot (\mathbf{r}_t - \mathbf{r}_{t'})} \kappa d\kappa d\Theta, \end{aligned} \quad (\text{A4})$$

where  $\boldsymbol{\kappa} = (\kappa_x, \kappa_y) = (\kappa \cos \Theta, \kappa \sin \Theta)$  is the wave number vector with magnitude  $\kappa$  and azimuthal direction  $\Theta$ . The roughness height standard deviation  $\sigma_\zeta$  is then given by

$$\sigma_\zeta^2 = C_{\zeta\zeta}(0) = \frac{1}{(2\pi)^2} \int_0^{2\pi} \int_0^\infty \mathcal{G}(\boldsymbol{\kappa}) \kappa d\kappa d\Theta, \quad (\text{A5})$$

when  $\langle \zeta \rangle = 0$ , as with the present case.

The coherence length scale for the rough surface in the  $x$  and  $y$  directions and its coherence area  $A_c$  can be expressed in terms of its correlation function as given by Eqs. (7)–(10) of Ref. 21 or Eqs. (A7) and (A8) of Ref. 23. For instance, the correlation lengths  $\ell_x$  and  $\ell_y$  of the random process in the  $x$  and  $y$  directions, respectively, are

$$\ell_x = \ell_c(\Theta = 0) + \ell_c(\Theta = \pi), \quad (\text{A6})$$

and

$$\ell_y = \ell_c(\Theta = \pi/2) + \ell_c(\Theta = 3\pi/2), \quad (\text{A7})$$

where  $\ell_c(\Theta)$  is the correlation length of the random process in any azimuthal direction  $\Theta$  given by<sup>24</sup>

$$\begin{aligned} \ell_c(\Theta) &= \frac{2(1/2\pi)^2 \int_0^\infty |G(\kappa, \Theta)|^2 \kappa d\kappa}{|(1/2\pi)^2 \int_0^{2\pi} \int_0^\infty G(\kappa, \Theta) \kappa d\kappa d\Theta|^2} \\ &= \frac{2(1/2\pi)^2 \int_0^\infty |G(\kappa, \Theta)|^2 \kappa d\kappa}{|C_{\zeta\zeta}(0)|^2}. \end{aligned} \quad (\text{A8})$$

The coherence length  $\ell_c$  defines a shape function for the random process as its wave number spans the  $2\pi$  azimuthal radians of  $\Theta$ . The coherence area of the process is given by

$$\begin{aligned} A_c &= \frac{(1/2\pi)^2 \int_0^{2\pi} \int_0^\infty |G(\kappa, \Theta)|^2 \kappa d\kappa d\Theta}{\left| (1/2\pi)^2 \int_0^{2\pi} \int_0^\infty G(\kappa, \Theta) \kappa d\kappa d\Theta \right|^2} \\ &= \frac{(1/2\pi)^2 \int_0^{2\pi} \int_0^\infty |G(\kappa, \Theta)|^2 \kappa d\kappa d\Theta}{|C_{\zeta\zeta}(0)|^2}. \end{aligned} \quad (\text{A9})$$

*Isotropic rough surface.* For an isotropic rough surface, Eq. (A4) for the correlation function reduces to

$$\langle \zeta(\mathbf{r}_t)\zeta(\mathbf{r}_{t'}) \rangle = \frac{1}{2\pi} \int_0^\infty \mathcal{G}(\boldsymbol{\kappa}) J_0(\kappa|\mathbf{r}_t - \mathbf{r}_{t'}|) \kappa d\kappa, \quad (\text{A10})$$

since its wave number spectrum  $\mathcal{G}(\boldsymbol{\kappa})$  is independent of the azimuth angle  $\Theta$ . The coherence radius  $\ell_c(\Theta)$  is a constant independent of azimuthal direction  $\Theta$  so that the corresponding coherence lengths in the  $x$  and  $y$  directions and coherence area are simply given by  $\ell_x = \ell_y = 2\ell_c$  and  $A_c = \pi\ell_c^2$ .

<sup>1</sup>M. S. Young and Y. C. Li, "A high precision ultrasonic system for vibration measurements," *Rev. Sci. Instrum.* **63**, 5435–5441 (1992).

<sup>2</sup>Y. Yamakoshi, J. Sato, and T. Sato, "Ultrasonic imaging of internal vibration of soft tissue under forced vibration," *IEEE Trans. Ultrason. Ferroelectr. Freq. Control* **37**, 45–53 (1990).

<sup>3</sup>J. M. Sabatier and N. Xiang, "An investigation of acoustic-to-seismic coupling to detect buried antitank mines," *IEEE Trans. Geosci. Remote Sens.* **39**, 1146–1154 (2001).

<sup>4</sup>W. R. Scott, J. S. Martin, and G. D. Larson, "Experimental model for a seismic landmine detection system," *IEEE Trans. Geosci. Remote Sens.* **39**, 1155–1164 (2001).

<sup>5</sup>N. Xiang and J. M. Sabatier, "An experimental study on antipersonnel landmine detection using acoustic-to-seismic coupling," *J. Acoust. Soc. Am.* **113**, 1333–1341 (2003).

<sup>6</sup>J. S. Martin *et al.*, "Ultrasonic displacement sensor for the seismic detection of buried land mines," *Proc. SPIE* **4742**, 606–616 (2002).

<sup>7</sup>A. G. Petculescu and J. Sabatier, "Air-coupled ultrasonic sensing of grass-covered vibrating surfaces; qualitative comparisons with laser Doppler vibrometry," *J. Acoust. Soc. Am.* **115**, 1557–1564 (2004).

<sup>8</sup>D. Fenneman, B. Libbey, and J. Martin, "Evaluation of an ultrasonic displacement sensor," *J. Acoust. Soc. Am.* **115**, 2416 (2004).

<sup>9</sup>W. P. Arnott and J. M. Sabatier, "Laser-Doppler vibrometer measurements of acoustic to seismic coupling," *Appl. Acoust.* **30**, 279–291 (1990).

<sup>10</sup>V. Arunchuk, A. K. Lal, C. F. Hess, and J. M. Sabatier, "Multi-beam laser Doppler vibrometer for landmine detection," *J. Op. Eng.* **45**, 104302 (2006).

<sup>11</sup>L. E. Drain, *The Laser Doppler Technique* (Wiley, Chichester, 1980).

<sup>12</sup>A. Kannath and R. J. Dewhurst, "Real-time measurement of acoustic field displacements using ultrasonic interferometry," *Meas. Sci. Technol.* **15**, N59–N66 (2004).

<sup>13</sup>W. R. Scott, J. C. Schroeder, and J. S. Martin, "An acousto-electromagnetic sensor for locating land mines," *Proc. SPIE* **3392**, 176–186 (1998).

<sup>14</sup>S. Rothberg and B. Halkon, "Laser vibrometry meets laser speckle," *Proc. SPIE* **5503**, 280–291 (2004).

<sup>15</sup>S. Rothberg, J. R. Baker, and N. A. Hallowell, "Laser vibrometry: pseudo-vibrations," *J. Sound Vib.* **135**, 516–522 (1989).

- <sup>16</sup>P. M. Morse and K. U. Ingard, *Theoretical Acoustics* (Princeton University Press, Princeton, NJ, 1986).
- <sup>17</sup>J. A. Ogilvy, *Theory of Wave Scattering from Random Rough Surfaces* (IOP, Bristol, 1991).
- <sup>18</sup>M. Abramowitz and I. A. Stegun, *Handbook of Mathematical Functions* (Dover, New York, 1972).
- <sup>19</sup>J. W. Goodman, *Statistical Optics* (Wiley, New York, 1985).
- <sup>20</sup>N. C. Makris, "The effect of saturated transmission scintillation on ocean acoustic intensity measurements," *J. Acoust. Soc. Am.* **100**, 769–783 (1996).
- <sup>21</sup>T. Chen, P. Ratilal, and N. C. Makris, "Mean and variance of the forward field propagated through three-dimensional random internal waves in a continental-shelf waveguide," *J. Acoust. Soc. Am.* **118**, 3560–3574 (2005).
- <sup>22</sup>L. Mandel and E. Wolf, *Optical Coherence and Quantum Optics* (Cambridge University Press, New York, 1995).
- <sup>23</sup>P. Ratilal and N. C. Makris, "Mean and covariance of the forward field propagated through a stratified ocean waveguide with three-dimensional random inhomogeneities," *J. Acoust. Soc. Am.* **118**, 3532–3559 (2005).
- <sup>24</sup>B. R. Frieden, *Probability, Statistical Optics, and Data Testing* (Springer, New York, 1936).
- <sup>25</sup>P. Beckmann and A. Spizzichino, *The Scattering of Electromagnetic Waves from Rough Surfaces* (Pergamon/Macmillan, New York, 1963).
- <sup>26</sup>J. C. Dainty (editor), "Laser Speckle and Related Phenomena," *Topics in Applied Physics*, Vol. 9 (Springer-Verlag, Berlin 1975).